

Application of Immersed Boundary Method to Variational Doppler Radar Analysis System (VDRAS)

Sheng-Lun Tai¹, Yu-Chieng Liou¹, Juanzhen Sun², Shao-Fan Chang¹

¹*Department of Atmospheric Sciences, National Central University, Jhongli, Taiwan*

²*National Center for Atmospheric Research, Boulder, Colorado, USA*

(Dated: 17 July 2014)

1 Introduction

The Variational Doppler Radar Analysis System (VDRAS) has been widely used for nowcasting (Crook and Sun, 2002, 2004) and quantitative precipitation forecast (QPF) (Sun and Zhang, 2008). Although many successful applications by VDRAS were presented in recent years, the lack of ability to resolve terrain effect degrades its performance when encounter the environment with complex topography. Tai et al. (2011) merged VDRAS 4DVAR analysis field with WRF model field and forecast by WRF model. They demonstrated that positive impact can be achieved by resolving terrain using WRF.

In order to improve the analysis system, Ghost-cell Immersed Boundary Method (GCIBM) (Tseng and Ferziger, 2003) is applied to the analysis system. For the model verification, two idealized experiments are conducted, including a two-dimensional linear mountain wave simulation and a three-dimensional leeside vortex simulation. Furthermore, preliminary real case experiments are also demonstrated after passing gradient check for the modified adjoint model, which are analyzed by both original-version VDRAS and modified one. The forecast performance of the new system is evaluated by radial wind observation and rain gauge data, the positive impacts are evident through the verifications.

2 The Variational Doppler Radar Analysis System (VDRAS)

The central process of VDRAS is the 4DVAR radar data assimilation, which includes a cloud-scale numerical model, the adjoint of the numerical model, a cost function, a minimization algorithm, and the specification of weighting coefficients. For details on each of these components, readers are referred to Sun and Crook (1997, 2001). The numerical model used to represent the convective-scale motion is anelastic, with Kessler-type warm rain microphysical parameterization.

There are six prognostic equations: the three velocity components (u , v , w), the liquid water potential temperature (θ_l), the total water mixing ratio (q_t), and the rainwater mixing ratio (q_r). The pressure (p) is diagnosed through a Poisson equation. The temperature (T) and the cloud water mixing ratio (q_c) are diagnosed from the prognostic variable.

3 Ghost-cell Immersed Boundary Method and the implementation

The immersed boundary method (IBM) has recently been demonstrated to be applicable to complex geometries in computational fluid dynamics (CFD). The Ghost-cell Immersed Boundary Method (GCIBM) is one variant of them and proposed by Tseng and Ferziger (2003), which can readily be implemented in any existing Cartesian grid code with staggered or non-staggered grids.

The “ghost-cell” is defined as the first grid point under the terrain surface. By giving the value that satisfies appropriate boundary conditions at every time step on those ghost cells, model implemented with GCIBM could simulate terrain effect reasonably well after integration. The numerical procedure for implementation of GCIBM is following:

1. Detect the terrain boundary and determine the physical and ghost cell domains in the 3-D model domain (Figure 1).
2. Interpolate from points in physical domain to get the value on image point of ghost-cell (as I point in Figure 1). And update ghost cell by imposing the boundary condition implicitly.
3. Integrate the nonlinear model (only physical domain grid points) and solve the pressure Poisson equation to obtain the forecast at next time step.
4. Update ghost-cell again by the new forecast field and certain boundary condition.

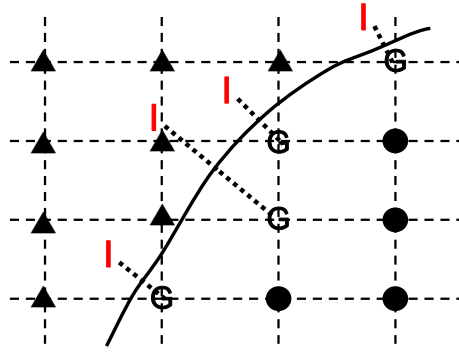


Figure 1: Schematic of computational domain with an immersed boundary. ▲, point in the physical domain, G, point in the ghost cell domain and I, the image point of ghost cell. Dotted lines are perpendicular to the immersed boundary.

In this study, we impose Neumann boundary condition whereas ghost-cell equals image point for variables of horizontal winds, liquid water potential temperature perturbation and mixing ratios of total water, cloud water and rainwater. For vertical velocity, the ghost-cell equals boundary condition as

$$w = u \frac{dh_t}{dx} + v \frac{dh_t}{dy} \quad (3.1)$$

where h_t represents terrain height at each ghost-cell grid. By repeating steps 2 to 4 as the model integration continues, the expected results will be gradually obtained.

4 Verification of forecast model

4.1 2-D Linear Mountain Wave

Linear mountain waves are often simulated for comparisons with the available analytic solution. The behavior of linear mountain wave has been studied by previous research and is summarized by Smith (1980). If the upstream wind speed is uniform (no vertical shear), the behavior of linear hydrostatic mountain wave can be described by the following equation

$$\frac{\partial^2 \delta}{\partial z^2} + l^2 \delta = 0 \quad (4.1)$$

If the atmosphere is isothermal, l (Scorer parameter) is constant,

$$l^2 = \frac{g}{C_p \bar{T} \bar{U}^2} - \frac{g^2}{4R^2 \bar{T}^2} \quad (4.2)$$

A bell-shaped mountain contour is specified as

$$z(x) = \frac{ha}{x^2 + a^2} \quad (4.3)$$

with an imposed linearized boundary condition $\delta(x, 0) = z$ at the surface, and the radiation boundary condition for the upper boundary. The solution subject to these boundary conditions is

$$\delta(x, z) = \left(\frac{\rho_0}{\bar{\rho}}\right)^2 ha \frac{a \cos lz - x \sin lz}{x^2 + a^2} \quad (4.4)$$

The analytical solution of perturbation horizontal and vertical velocities are calculated from these relation

$$u' = -\frac{\bar{U}}{\bar{\rho}} \frac{\partial \bar{\rho} \delta}{\partial x}, w' = \bar{U} \frac{\partial \delta}{\partial x} \quad (4.5)$$

In this test, the parameters that satisfy the requirements are chosen as following: $T = 250K$, $U = 20 \text{ ms}^{-1}$, $a = 10 \text{ km}$, $h = 1 \text{ m}$. The length of horizontal domain is 202 km with grid interval 2 km, and 20 km for domain height with constant vertical spacing as 0.2 km. The sponge layer is set at the upper half domain. Results from the analytical solution and model simulation obtained at $Ut/a = 60$ for perturbation vertical velocity are displayed in Figure 2. As evidenced in Figure 2, the numerical and analytical solutions agree well in both wave length and magnitude.

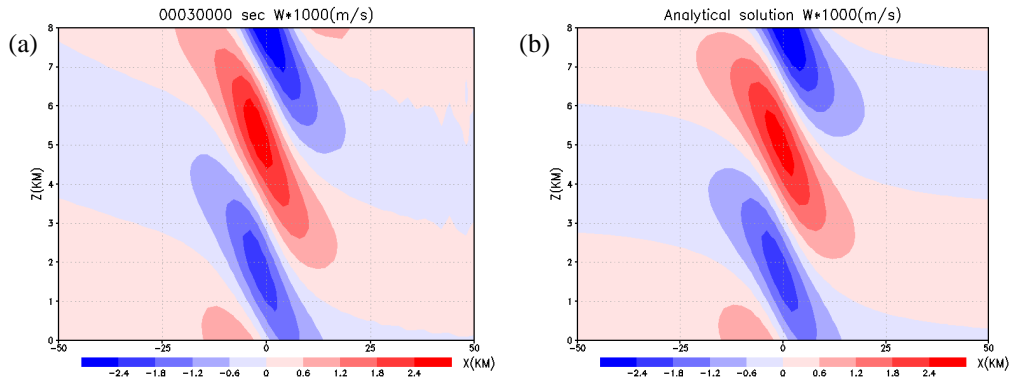


Figure 2: The vertical velocity field of 2-D linear mountain wave. (a) Simulated result at 30000 seconds ($Ut/a = 60$), (b) Analytical solution; both the magnitudes have been amplified by 1000.

4.2 3-D Lee Vortex simulation

In addition to two-dimensional simulation, the three-dimensional lee-vortex simulation was also conducted for more examination. The model initialized with horizontal isentropic surfaces, corresponding to a uniform Brunt–Väisälä frequency of $N = 0.01 \text{ s}^{-1}$ and wind speed of $U = 6 \text{ ms}^{-1}$. A bell-shaped mountain of 3 km height and half-width 10 km is located at left of domain center, and the distance from center is quarter of x-direction domain size. The horizontal domain has constant grid size of 2 km and contains 151 and 121 uniform grids in the x and y directions, respectively. In the vertical direction, there are 40 levels with interval of 0.25 km. In order to prevent reflection of vertical propagating gravity waves, sponge layers are employed in the upper portion of the model domain.

From the above related parameters, the Froude number (U/NH) equals 0.2, which is in the interval (under 0.5) that reversed flow and vortices are expected to appear in the low-level of lee side (Smolarkiewicz and Rotunno, 1989). It was also mentioned that the process occurs without viscosity-boundary layer.

The simulated result at $Ut/a = 7.2$, as shown in Figure 3a, is compatible with results at $Ut/a = 9$ in Smolarkiewicz and Rotunno (1989) and $Ut/a = 5$ by Schär and Durran (1997). As the time evolves, the lee vortices developed toward downstream and become elongated as shown in Figure 3b. Since the shape and size of the lee vortex are related to the advection scheme and intensity of numerical dissipation, exact comparison is not so meaningful. Overall, the simulated flow evolution is mostly consistent with previous studies.

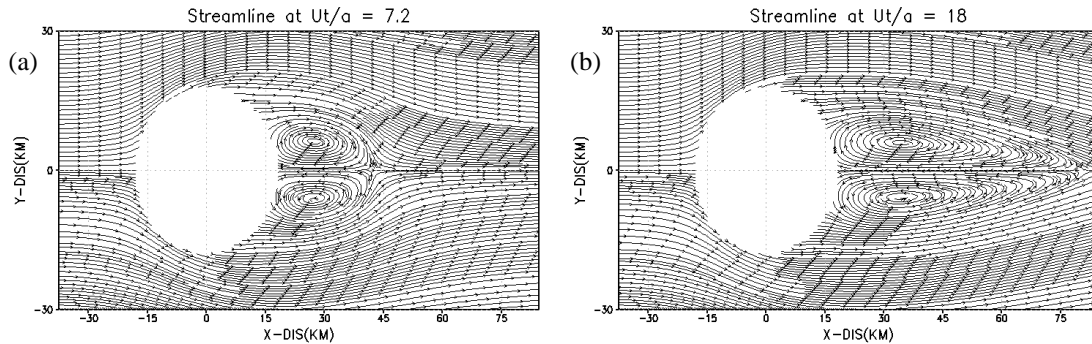


Figure 3: 3-D lee vortex model simulation results at (a) $Ut/a = 7.2$ and (b) $Ut/a = 18$. The model height is at 0.375 km.

5 Adjoint model modification and gradient check

Since the forward model has been modified based on IBM, the adjoint model must be changed accordingly. The main parts which have been changed are: (1) prognostic equation: advection, diffusion; (2) cost function calculation: observation terms (rainwater mixing ratio and radial velocity), background terms and smoothing term (spatial and temporal).

Still, the modification on adjoint model should also be verified. The method for the verification follows the gradient check procedure in Sun and Crook (1997). Gradient value $\Phi(\alpha)$ can be calculated through the equation below

$$\Phi(\alpha) = \frac{F(x_0 + \alpha h) - F(x_0)}{\alpha G h} \quad (5.1)$$

where F and G are the nonlinear model and the tangent linear model (TLM) operators, respectively. The quantity h is a normalized random vector and α is a scalar. If the TLM approximates the nonlinear model well, one should expect to obtain a value of $\Phi(\alpha)$ close to unity for small values of α at any particular point. Here we show $\Phi(\alpha)$ summed over all points in the domain. Figure 4 shows the various gradient values when introducing perturbation in different orders. From the results, the

modified adjoint model successfully passes the gradient check, since the gradient values are all very close to 1 at various orders of perturbation.

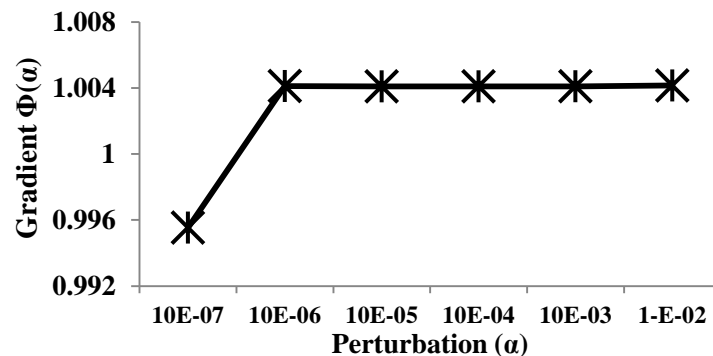


Figure 4: Gradient check results. Star (*) shows the corresponding gradient value $\Phi(\alpha)$ when different orders of perturbation α is introduced.

6 Preliminary Experiment of Real Case

Although the two verification simulations have shown the ability on simulating reasonable terrain effect, investigation is still needed when the whole modified system is applied to a real case with complex terrain and additional moisture. Assimilation experiments are conducted by using both original version VDRAS and modified VDRAS, therefore we could directly understand how much change is made in analysis and forecast after the implementation of IBM.

The case selected for assimilation is from IOP8 of South-West Monsoon Experiment (SoWMEX), which has been studied by using original version VDRAS in Tai et al. (2011). The line convections embedded in a Mei-Yu front passed through southwestern Taiwan, resulted in heavy rainfall especially on the windward (southwestern) side.

The model domain for both experiments contains 230×200 grid points in horizontal and 50 vertical levels with $\Delta x = \Delta y = 2$ km and $\Delta z = 0.25$ km. The assimilation strategy and following forecast are depicted in Figure 5. Basically, the assimilation procedure starts at 1022 UTC June 14 2008 and ends at 1102 UTC by using both original VDRAS (hereafter named VDRAS) and modified VDRAS (IBMVDAS). During this period of time, two assimilation windows are included and also a forecast inserted in between. Three radars located at southwestern Taiwan (RCKT, RCCG and SPOL) are assimilated with background field prepared by radiosonde and surface mesonet station observations. After the assimilation procedure is accomplished, the analysis field is integrated by the full nonlinear model with (IBMVDAS) and without (VDRAS) terrain for two hours long.

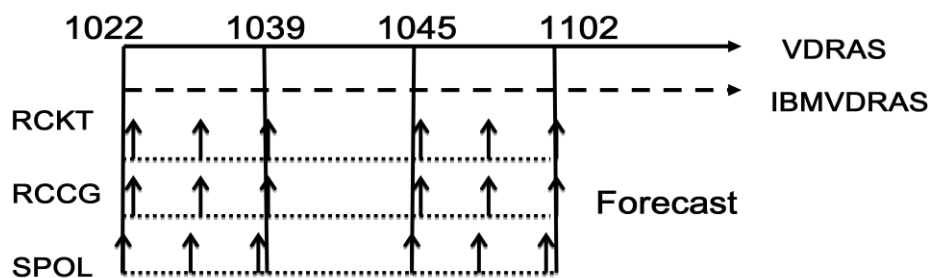


Figure 5: Assimilation strategy and experiment design for the real case experiments. Volume data of three radars (RCKT, RCCG and SPOL) are assimilated. The first assimilation cycle is from 1022 UTC to 1039 UTC 14 2008 and 1045 UTC to 1102 for the second cycle. A period of forecast is arranged at between. Forecast period is followed at the end of second cycle.

6.1 Analysis field

Since the experiments are just preliminary results, only some variables in analysis field (UTC 1102) are examined. From the meridional (V) wind field at 1.125 km height level, the terrain effects are clearly shown by those detail structure around terrain especially the leeside in the IBMVDAS results (Figure 6b). The decreasing wind speed in the valleys and the speeding up out of valleys are relatively reasonable. Figure 7 shows the amount of rainwater mixing ratio and also wind vector at 1.125 km height level. In addition to the main rainband near coast, IBMVDAS result show some cells develop at windward side of Central Mountain Range mainly due to the mechanical lifting. The above evidences give us the pictures that the terrain effects can be retrieved nicely through the 4DVAR cycles, but the need of verification is still for sure.

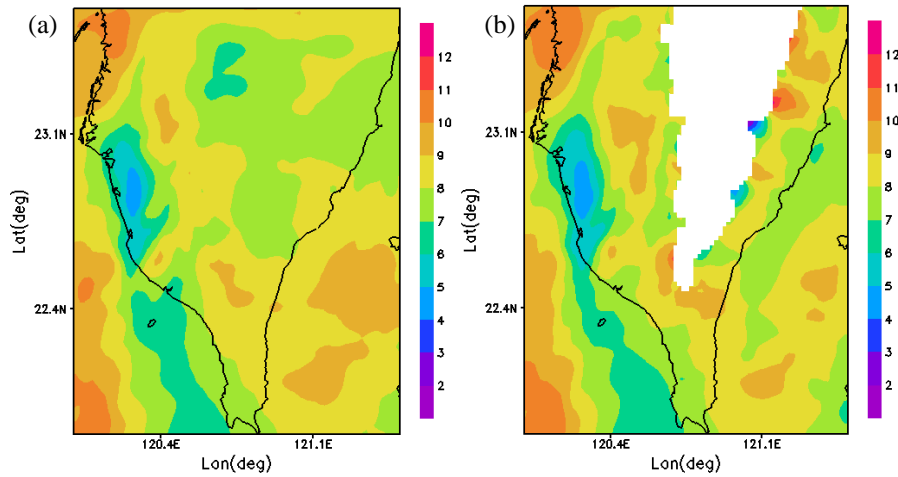


Figure 6: V-wind analysis results of both (a) VDRAS and (b) IBMVDRAS experiments. Shaded color represents wind speed in unit of ms^{-1} .

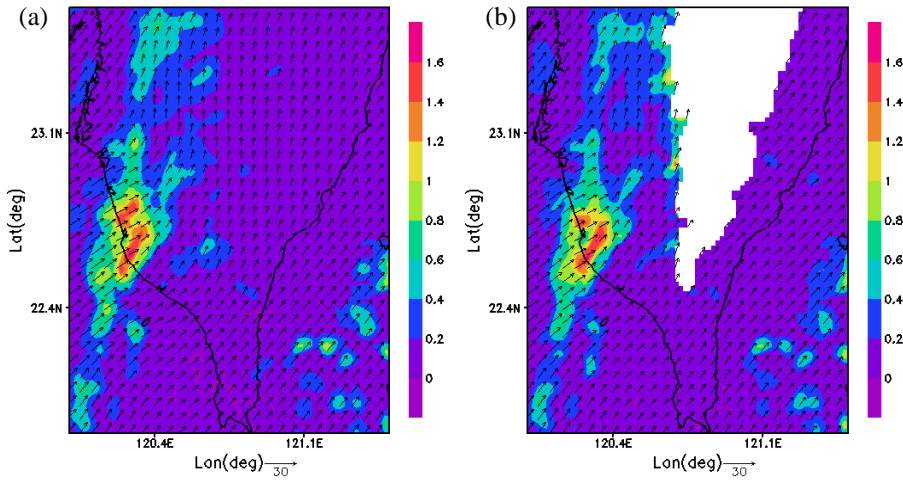


Figure 7: Rainwater mixing ratio and wind vector analysis results of both (a) VDRAS and (b) IBMVDRAS experiments. Shaded color represents the amount of rainwater mixing ratio in unit of gkg^{-1} .

6.2 Verification

The verifications are not only in analysis but also forecast. Here we provide some results about dynamical and rainfall predictions, the thermodynamical parts are left for our future works.

6.2.1 Wind forecast

For the wind verification, radial wind observed by radar is the most extensive one. Here we choose the data from RCCG radar (located at coast of southwestern Taiwan) for the use of verification. The volume data is interpolated to Cartesian coordinate in the same resolution with previous model domain for the convenience of comparison. Since the radar only observes radial wind, Cartesian model simulated velocity components (u , v , w) are calculated back to radial component (V_r) by following equation

$$V_r = u \frac{x - x_{rad}}{r} + v \frac{y - y_{rad}}{r} + (w - V_T) \frac{z - z_{rad}}{r} \quad (6.1)$$

V_T is the terminal velocity of the precipitation. Here, r is the distance between a grid point (x , y , z) and the RCCG radar location (x_{rad} , y_{rad} , z_{rad}). To quantitatively understand the performance of both VDRAS and IBMVDRAS, we calculate the mean absolute error difference (MAED) as following

$$\text{MAED} = \frac{\sum_{i=1}^n [|N_i - R_i| - |Y_i - R_i|]}{n} \quad (6.2)$$

Where N_i , Y_i represent model grid radial wind value of VDRAS and IBMVDRAS, respectively. R_i is the RCCG observed radial wind at the same grid point i , n means the number of observations on Cartesian grid point. When MAED is larger than zero, IBMVDRAS forecast is better than VDRAS. Otherwise, negative value means the VDRAS is better.

In order to investigate the relative error variation at vertical levels, the MAED is calculated at different model levels. Figure 8 shows the MAED for three simulation time (UTC 1100, 1200, 1300) within 10 model levels (below 2.375 km

height). It's obvious that the improvement increases at low levels as forecast time evolves, suggested that the modified model can reasonably resolve the terrain effect by continuous model integration.

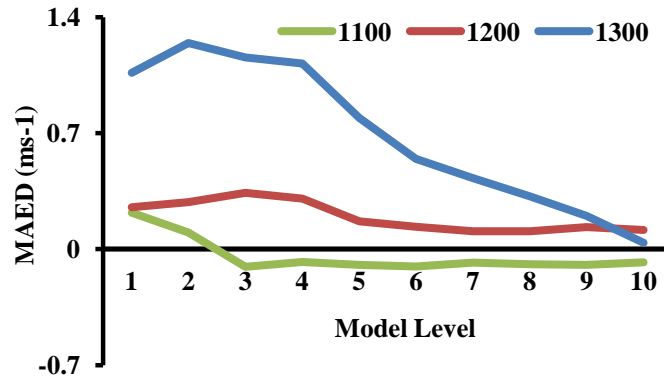


Figure 8: MAED (ms^{-1}) calculated in different vertical levels for three forecast times (UTC 1100, 1200 and 1300).

6.2.2 Precipitation forecast

For more examination on precipitation forecast, two-hour quantitative precipitation forecasts (QPF) by both experiments are verified by rain gauges on the ground. At first, we compute the rain rate RR for each horizontal grid point on the surface-nearest model layer as follows

$$\text{RR} = \frac{q_r(V_T - w)\rho_a}{\rho_w} \quad (6.3)$$

where q_r (kg kg^{-1}) is the rainwater mixing ratio; ρ_a and ρ_w (kg m^{-3}) represent the air and water densities, respectively; V_T (ms^{-1}) stands for the terminal velocity and w is vertical velocity (ms^{-1}). Since RR has the unit meters per second, it is converted to the rainfall amount (mm) for each model time step (ΔT) by

$$\text{PRE} = \text{RR} \times 1000 \times \Delta T \quad (6.4)$$

Figure 9 displays the two-hour accumulated rainfall amounts from VDRAS, IBMVDRAS and the difference between both experiments. That reveals the topography actually plays an important role in the development of convective cells, which then cause some slightly decrease of precipitation on the northern ridge of CMR as shown in Figure 9c. In the mean time, strengthened convective cells in windward slope increase precipitation significantly.

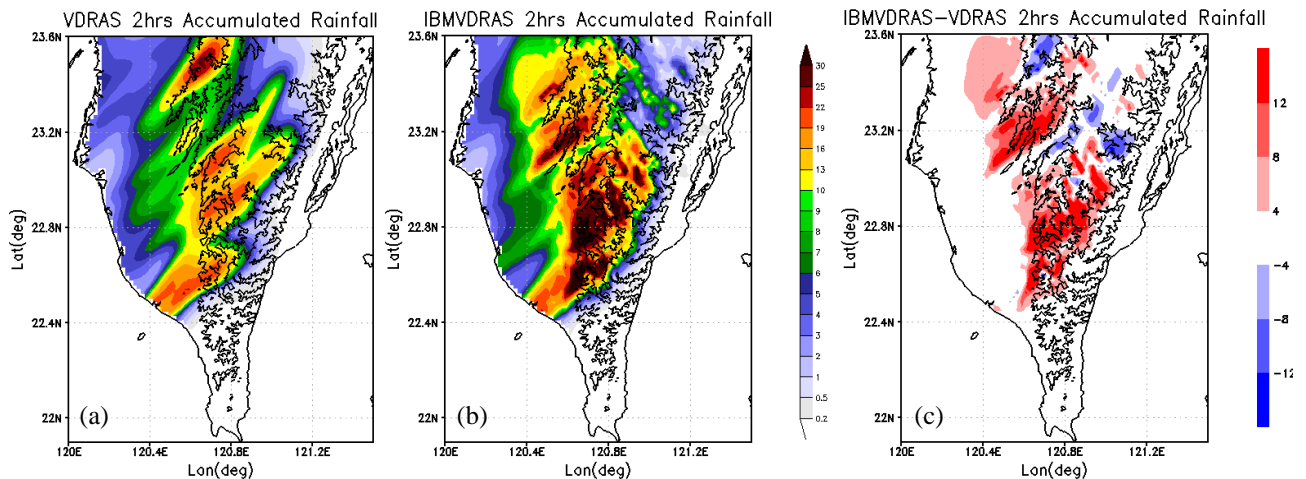


Figure 9: 2 hours accumulated rainfall amount (mm) for: (a) VDRAS experiment, (b) IBMVDRAS experiment. (c) The difference between IBMVDRAS and VDRAS (IBMVDRAS minus VDRAS).

For the purposes of comparison, the predicted rainfall amounts distributed at the model grid points are interpolated to each rain gauge site. Then, the equitable threat score (ETS) proposed by Schaefer (1990) is utilized to provide a quantitative comparison in QPF accuracy under different scenarios. This index is defined as

$$\text{ETS} = \frac{H - R}{F + O - H - R} \quad (6.5)$$

Where H is the number of correctly predicted points above a certain threshold, F stands for the number of forecast points above a threshold, O represents the number of observed points above a threshold, and R is the number of hits by chance, which can be written as

$$R = \frac{F \times O}{N}, \quad (6.6)$$

where N is the total number of points in the verification domain. When ETS = 1, it implies a perfect forecast. Fig. 10a shows the ETS for both VDRAS and IBMVDRAS experiments. The IBMVDRAS obviously performs better than VDRAS in all thresholds (10, 14, 18 and 22 mm). Thus, it is believed that the implementation has positive impact on the precipitation forecast. The satisfactory results from IBMVDRAS are encouraging, since the rain gauges distribution is much denser in plain than in mountainous area. Root mean square error (RMSE) calculated under the same thresholds are also presented in Figure 10b, which is again to prove the considerable improvement for the new assimilation system.

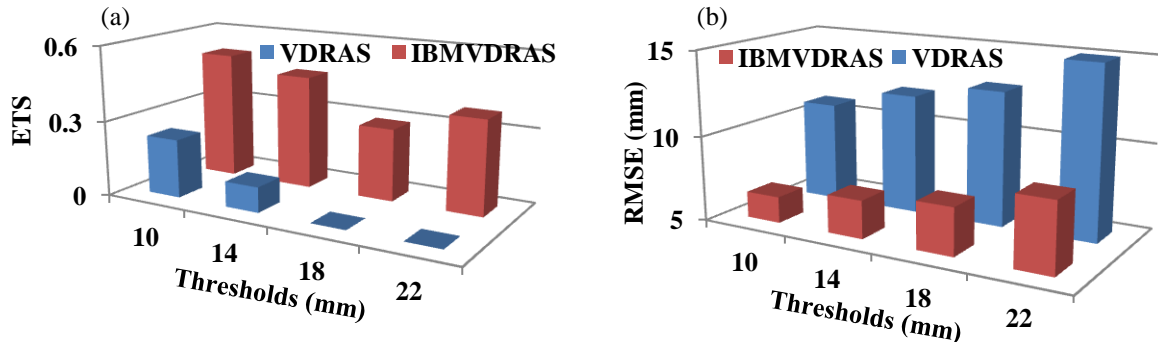


Figure 10: The (a) ETS and (b) RMSE calculated from 2 hour accumulated precipitation forecasts by VDRAS (blue bar) and IBMVDRAS (red bar) experiments at different thresholds (10, 14, 18 and 22 mm).

Acknowledgement

This research is supported by Central Weather Bureau of Taiwan, under Grant MOTC-CWB-102-M-11 and MOTC-CWB-103-M-06.

References

- Crook, N. A., and J. Sun, 2002: Assimilating radar, surface, and profiler data for the Sydney 2000 forecast demonstration project, *J. Atmos. Oceanic. Technol.*, **19**, 888-898.
- , and —, 2004: Analysis and Forecasting of the Low-Level Wind during the Sydney 2000 Forecast Demonstration Project. *Wea. Forecasting*, **19**, 151-167.
- Schaefer, J. T., 1990: The critical success index as an indicator of warning skill. *Wea. Forecasting*, **5**, 570-575.
- Schär, C. and Dale R. Durran, 1997: Vortex Formation and Vortex Shedding in Continuously Stratified Flows past Isolated Topography. *J. Atmos. Sci.*, **54**, 534-554.
- Smith, R. B., 1980: Linear theory of stratified hydrostatic flow past an isolated mountain. *Tellus*, **32**, 348-364.
- Smolarkiewicz, P. K., and R. Rotunno, 1989: Low Froude number flow past three-dimensional obstacles. Part I: Baroclinically generated lee vortices. *J. Atmos. Sci.*, **46**, 1154-1164.
- Sun, J. and N. A. Crook, 1997: Dynamic and microphysical retrieval from Doppler radar observations using a cloud model and its adjoint. Part I: Model development and simulated data experiments. *J. Atmos. Sci.*, **54**, 1642-1661.
- , and —, 2001: Real-time low-level wind and temperature analysis using single WSR-88D data. *Wea. Forecasting*, **16**, 117-132.
- , and Y. Zhang, 2008: Analysis and prediction of a squall line observed during IHOP using multiple WSR-88D observations. *Mon. Wea. Rev.*, **136**, 2364-2388.
- Tai, S. L., Y. C. Liou, J. Sun, S. F. Chang, and M. C. Kuo, 2011: Precipitation Forecast using Doppler Radar Data, a Cloud Model with Adjoint, and the Weather Research and Forecasting Model – Real Case Studies during SoWMEX in Taiwan, *Wea. Forecasting*, **26**, 975-992.
- Tseng, Y. and J. Ferziger, 2003: A ghost-cell immersed boundary method for flow in complex geometry. *J. Comput. Phys.*, **192**, 593-623.